Chinese Journal of Chemical Engineering 81 (2025) 115–127

Contents lists available at ScienceDirect

Chinese Journal of Chemical Engineering

journal homepage: www.elsevier.com/locate/CJChE

Full Length Article

A three-dimensional CFD numerical simulation study on pressurized oxy-fuel gasification of poultry manure in an industrial-scale gasifier

Qinwen Liu [1, 2], Guoqing Lian [1], Wenli Dong [3], Yu Su [2], Wei Quan Leong [4], Chi-Hwa Wang [5], Wenqi Zhong [1, *]

[1] School of Energy and Environment, Southeast University, Nanjing 210096, China
[2] State Key Laboratory of Low-carbon Smart Coal-fired Power Generation and Ultra-clean Emission, Southeast University, Nanjing 210096, China
[3] Special Equipment Safety Supervision Inspection Institute of Jiangsu Province, Nanjing 210036, China
[4] Acropower Pte. Ltd.11 Woodlands Terrace 738436, Singapore
[5] Department of Chemical and Biomolecular Engineering, National University of Singapore, 117585, Singapore

ARTICLE INFO

Article history:
Received 2 January 2025
Received in revised form
28 February 2025
Accepted 3 March 2025
Available online 8 March 2025

Keywords:
Oxy-fuel gasification
Pressurized gasification
Poultry manure
Carbon negative
CFD numerical simulation

ABSTRACT

As a renewable energy source, the thermal conversion of poultry manure, is a promising waste treatment solution that can generate circular economic outputs such as energy and reduce greenhouse gas emissions. Currently, pressurized gasification of poultry manure is still a novel research field, especially when combined with a novel technological route of oxy-fuel gasification. Oxy-fuel gasification is a newly proposed and promising gasification technology for power generation that facilitates future carbon capture and storage. In this work, based on a commercially operated industrial-scale chicken manure gasification power plant in Singapore, we presented an interesting first exploration of the coupled pressurization technology for oxy-fuel gasification of poultry manure using CFD numerical simulation, analyzed the effects of pressure and oxygen enrichment concentration as well as the coupling mechanism between them, and discussed the conversion and emission of nitrogen- and sulfur-containing pollutants. The results indicate that under oxy-fuel gasification condition (Oxy-30, *i.e.*, 30%O_2/70%CO_2), as the pressure increases from 0.1 to 0.5 MPa, the CO concentration in the syngas increases slightly, the H_2 concentration increases to approximately 25%, and the CH_4 concentration (less than 1%) decreases, resulting in an increase in the calorific value of syngas from 5.2 to 5.6 MJ·m^{-3}. Compared to atmospheric pressure conditions, a relatively higher oxygen-enriched concentration interval (Oxy-40 to Oxy-50) under pressurized conditions is advantageous for autothermal gasification. Pressurization increases NO precursors production and also promotes homogeneous and heterogeneous reduction of NO, and provides favorable conditions for self-desulfurization. This work offers reference for the realization of a highly efficient and low-energy-consumption thermochemical treatment of livestock manure coupled with negative carbon emission technology.

© 2025 The Chemical Industry and Engineering Society of China, and Chemical Industry Press Co., Ltd. All rights are reserved, including those for text and data mining, AI training, and similar technologies.

1. Introduction

As the global population grows, poultry play an increasingly important role in ensuring global food security, becoming the most consumed livestock commodity in the world [1]. For example, in 2022, 16.14 billion poultry were slaughtered in China; in 2023, the poultry production in the US was 52.58 billion pounds. At the same time, the global demand for sustainable energy is also increasing. As a renewable energy source, the thermal conversion of poultry manure, is a promising waste treatment solution that can generate circular economic outputs such as energy and reduce greenhouse gas emissions. Moreover, the thermal conversion method of treatment can also avoid the various side effects of traditional poultry manure treatment methods (returning to farmland and composting), such as eutrophication and pathogen transmission. In addition, the low carbon to nitrogen ratio of poultry manure itself poses a significant technical barrier to biogas production, which is one of the technical issues that have to be considered [1].

Gasification is receiving increasing attention in this waste-to-energy area. Gasification is a thermo-chemical conversion under relatively oxygen-deprived conditions, which can effectively inhibit the formation of toxic pollutants on the one hand and eliminate

* Corresponding author.
E-mail address: wqzhong@seu.edu.cn (W. Zhong).

https://doi.org/10.1016/j.cjche.2025.03.001
1004-9541/© 2025 The Chemical Industry and Engineering Society of China, and Chemical Industry Press Co., Ltd. All rights are reserved, including those for text and data mining, AI training, and similar technologies.

potential pathogenic hazards on the other hand [2], and ultimately produces valuable gases (syngas) and solid products (biochar and ash) for use in a wide range of applications such as power generation, construction, agriculture, catalysis, and so on [3]. Commercial coal gasifiers are typically operated at high pressures. Because pressurization not only increases the gasification rate, but also helps to reduce the power consumption for compressing the syngas to high pressure before the gas turbine combustion chamber [4]. Currently, pressurized gasification of poultry manure is still a novel research field, especially when it is coupled with a novel technological route of oxy-fuel gasification.

Oxy-fuel gasification is a newly proposed and promising gasification technology for power generation that facilitates future carbon capture and storage. This concept uses a mixture of CO_2 and O_2 to replace the use of air in combustion and gasification systems [5]. In this system, the air separation unit separates air to obtain O_2, which is then mixed with circulating CO_2 as a gasifying agent. The syngas produced by gasification is subsequently used in oxy-fuel combustion to generate electricity. Since the process is nitrogen free, the exhaust gas from combustion is mainly CO_2, of which a portion is recycled to the inlet of the process and the remaining portion can be used for sequestration or utilization. This system is an adaptation and extension of the oxy-fuel combustion technology route to achieve negative CO_2 emissions by combining carbon capture with oxy-fuel gasification and combustion, which is important for mitigating energy issues and environmental problems. In addition, it is predicted from the findings of the oxy-fuel combustion system analysis that the use of pressurized gasification and combustion in this process facilitates the gradient utilization of pressure, which can improve the system economics [6].

The current work for this novel field is still in the stage of theoretical system analysis and small-scale experiments. For example, Tan *et al.* [7] proposed a power generation scheme combining oxy-fuel combustion and biomass integrated gasification combined cycle (BIGCC) with CO_2 and H_2O as gasifying agents. The BIGCC system is derived from the coal-based IGCC concept, which integrates biomass gasification with a combined cycle of gas and steam turbines [8]. They introduced the oxy-fuel combustion technology into the BIGCC system to realize negative CO_2 emissions, and evaluated the cost of power generation, reporting a levelized cost of electricity (LCOE) of 0.17 USD·kWh^{-1} for the designed system. In their study, the influence of CO_2 content in the gasifying agent on the syngas composition was investigated. It was found that at a CO_2/C mole ratio of 1.0, the volume fraction of produced syngas consisted of approximately 50% CO, 30% H_2, and 20% CO_2. Spiegl *et al.* [5] investigated the operability and performance of oxy-fuel gasification of coal and coal/biomass mixtures on the spouted-bed gasifier, which is one of the few experimental studies available on oxy-fuel gasification and contributes to the discussion of the mechanisms. They found that higher temperatures or CO_2/C ratios are necessary to further increase carbon conversion.

However, there is currently limited research on numerical simulation of this emerging technology [9], and to the best of our knowledge, there has been no numerical simulation study on pressurized oxy-fuel gasification. There are a number of numerical simulations of high-pressure gasification systems that can provide a reference for pressurized oxy-fuel gasification (not limited to computational fluid dynamics (CFD) simulations). For example, Lei *et al.* [10] employed reactive force field molecular dynamics (ReaxFF MD) simulation to study the release behavior of gaseous sulfur during pressurized gasification and found that the elevated pressure reduced the main gaseous sulfur emissions and improved the possibility of coal char sulfur formation. Samani *et al.* [11] presented results from experimental and simulation studies on an oxygen-blown, steam-injected, pressurized (0.82 MPa) entrained flow gasification reactor with pulverized lignin pellets as feedstock and explored the impacts of reactor temperature, steam-to-biomass ratio, equivalence ratio, and the lignin particle size distribution on the gasification process. Yao *et al.* [12] employed the multiphase particle-in-cell (MP-PIC) model to study the pressure effects on the coal catalytic hydrogasification (CCHG) performance, and found the optimal interrelationship between pressure, particle size, and gas velocity, which provides useful guidance for the scale-up of the CCHG reactor. In addition, the three-dimensional (3D) CFD numerical simulation work for biomass gasification itself is also very limited.

In this work, based on a commercially operated industrial-scale chicken manure gasification power plant in Singapore, we adopted a numerical simulation approach to carry out an interesting first exploration of the coupled pressurization technology for oxy-fuel gasification of poultry manure, analyzed the effects of pressure and oxygen enrichment concentration in an industrial-scale downdraft fixed-bed gasifier as well as the coupling mechanism between them, and discussed the conversion and emission of nitrogen- and sulfur-containing pollutants in the process. Previously, our series of work [13] has explored CFD numerical simulation method for commercial-scale fixed-bed gasifier and discussed the differences between atmospheric air gasification and oxy-fuel gasification.

2. Model

2.1. Model construction

With the development of multiphase flow computational fluid dynamics, CFD numerical simulation methods can obtain details that cannot be obtained experimentally, predict results under a wider range of conditions, and design optimized reactor structures. However, at present, there are very few 3D Euler–Lagrange simulations for large commercial gasifiers, and most of the models are one- or two-dimensional [14]. And the conventional Euler–Lagrange methods (*e.g.*, computational fluid dynamics–discrete element method (CFD–DEM), dense discrete phase model (DDPM)) require extremely high computer arithmetic and storage capacity, making it difficult to achieve efficient simulation of large gasifiers. The MP-PIC method is similar to CFD–DEM but differs in its handling of particle interactions. Unlike CFD–DEM, which explicitly resolves particle collisions, MP-PIC approximates the collective behavior of particles by mapping their properties onto a Eulerian grid to compute the continuous particle stress field. Besides, the MP-PIC scheme uses computational particle swarm instead of real particles and no longer tracks each individual particle. While this approach may reduce accuracy compared to CFD–DEM, it significantly enhances computational efficiency, making it well-suited for large-scale industrial simulations. At present, a few large-scale gasifier simulations [9,15] have successfully applied the MP-PIC method, proving its applicability.

Therefore, the MP-PIC scheme, based on the Euler–Lagrange framework, was employed in this study. This approach introduces particle normal stress to describe interactions between particles. The stress gradient for particles is calculated on the Eulerian grid and then interpolated back to the discrete particles. The particle stress is a monotonically increasing function of the particle volume fraction, being zero when the particle volume fraction is zero. Collisions between particles are simulated using the particle normal stress, τ_p, which is expressed as Eq. (1). The model also assumes that in the case of close packing, multiple collisions occurring within the hydrodynamic computation interval will move the solid to release high stress, but these collisions will limit the motion to a range close to the average velocity of the particle mixture [16].

$$\tau_p = \frac{P_s \varepsilon_p^{\beta}}{\max\left[\varepsilon_{cp} - \varepsilon_p, \delta(1-\varepsilon_p)\right]} \quad (1)$$

where, P_s is a constant with units of pressure, ε_{cp} is the particle volume fraction at close packing, β is a constant ranging from 2 to 5, δ is a very small number with a magnitude of 10^{-7}.

The properties of computational particles are interpolated onto the Eulerian grid using an interpolation operator, and then interpolated back to the discrete particle positions after the computation. This process is implemented using a trilinear interpolation operator, where the interpolation algorithm is the product of interpolation operators in the *x*, *y*, and *z* directions [17]. For example, when the particle is located at the position $\boldsymbol{x}_p$ (x_p, y_p, z_p), the interpolation operator in the *x* direction for the computational cell ζ has the following properties (Eq. (2)). The interpolation operators in the *y* and *z* directions fulfill the similar conditions. The particle volume fraction is obtained by interpolating the discrete particles to the Eulerian grid, and the particle volume fraction in the computational cell ζ is calculated using Eq. (3). According to the conservation of volume fraction, the sum of the volume fractions of the fluid and particle phases is equal to 1, *i.e.*, $\varepsilon_p + \varepsilon_g = 1$.

$$S_{\xi}^{x}(x_p) = \begin{cases} 0, x_{\xi-1} \geq x_p \geq x_{\xi+1} \\ 1, x_p = x_{\xi} \end{cases} \quad (2)$$

$$\varepsilon_{p\zeta} = \frac{1}{V_{\zeta}} \sum_{k}^{N_p} \frac{m_{pk}}{\rho_{pk}} n_{pk} S_{p\zeta k} \quad (3)$$

where, V_{ζ} is the volume of the computational cell ζ, n_p is the number of real particles contained in the computational particle, N_p is the total number of computational particles in the grid cell, $S_{p\zeta}$ is the interpolation operator.

In addition, this study assumes that the temperature inside the particles is uniform, that chemical reactions inside the particles do not release heat, and that the heat release from reactions occurring on the particle surface can be neglected. Only the heat transferred from the gas phase to the particle phase is considered for the surface energy balance. The energy equation for the particle phase is given by Eq. (4). The exchanges of mass, momentum, and energy between the gas and particle phases are implemented by setting source terms in the governing equations for the gas phase.

$$C_V \frac{dT_p}{dt} = \frac{1}{m_p} \frac{\lambda_g Nu}{d_p} A_p (T_g - T_p) \quad (4)$$

The detailed modeling process refers to our published series of work [13], which developed a 3D Euler–Lagrange model for chicken manure gasification in an industrial fixed-bed gasifier. Tables 1 and 2 summarize the governing equations for the gas and solid phases, respectively.

In the downdraft fixed-bed gasifier, poultry manure undergoes four sub-processes of drying, pyrolysis, oxidation, and reduction in sequence during its downward movement. Drying and pyrolysis mainly rely on heat transfer from the lower fuel layer. In a continuously feeding gasifier, drying, pyrolysis and combustion occur almost simultaneously. In modeling the chemical reactions of chicken manure gasification, we considered CH_4 oxidation, H_2 oxidation, steam reforming, CO oxidation, water–gas shift, and tar combustion reactions for the homogeneous reactions, and considered the complete and incomplete oxidation of char, Boudouard reaction, steam gasification, and methanation reaction for heterogeneous reactions. In addition, we also considered the conversion of nitrogen and sulfur pollutants. During gasification, nitrogen- and sulfur-containing

Table 1
Gas-phase governing equations.

Continuity equation

$$\frac{\partial(\varepsilon_g \rho_g)}{\partial t} + \nabla\cdot(\varepsilon_g \rho_g \boldsymbol{u}_g) = \delta\dot{m}_p$$

Momentum equation

$$\frac{\partial(\varepsilon_g \rho_g \boldsymbol{u}_g)}{\partial t} + \nabla\cdot(\varepsilon_g \rho_g \boldsymbol{u}_g \boldsymbol{u}_g) = -\nabla p + \boldsymbol{F} + \varepsilon_g \rho_g \boldsymbol{g} + \nabla\cdot(\varepsilon_g \tau_g)$$

Transport equation

$$\frac{\partial(\varepsilon_g \rho_g Y_{g,i})}{\partial t} + \nabla\cdot(\varepsilon_g \rho_g Y_{g,i} \boldsymbol{u}_g) = \nabla\cdot(\rho_g D \varepsilon_g \nabla Y_{g,i}) + \delta\dot{m}_{i,\mathrm{chem}}$$

$$p_i = \frac{\rho_i RT}{Mw_i}$$

Energy equation

$$\frac{\partial(\varepsilon_g \rho_g h_g)}{\partial t} + \nabla\cdot(\varepsilon_g \rho_g h_g \boldsymbol{u}_g) = \varepsilon_g\left(\frac{\partial p}{\partial t} + \boldsymbol{u}_g\cdot\nabla p\right) + \Phi - \nabla\cdot(\varepsilon_g \boldsymbol{q}) + \dot{Q} + S_h + \dot{q}_D$$

Large eddy simulation turbulence model

$$\tau_{g,ij} = \mu_t\left(\frac{\partial u_{g,i}}{\partial x_j} + \frac{\partial u_{g,j}}{\partial x_i}\right) - \frac{2}{3}\mu_t \delta_{ij} \frac{\partial u_{g,k}}{\partial x_k}$$

$$\mu_t = C\rho_g \Delta^2 \sqrt{\left(\frac{\partial u_{g,i}}{\partial x_j} + \frac{\partial u_{g,j}}{\partial x_i}\right)^2}$$

The source term in the gas-phase mass equation

$$\delta\dot{m}_p = -\iiint f \frac{dm_p}{dt} dm_p d\boldsymbol{u}_p dT_p$$

The momentum transfer rate in the gas-phase momentum equation

$$\boldsymbol{F} = -\iiint f\{m_p\left[D_p(\boldsymbol{u}_g - \boldsymbol{u}_p) - \frac{\nabla p}{\rho_p}\right] + \frac{dm_p}{dt}\boldsymbol{u}_p\} dm_p d\boldsymbol{u}_p dT_p$$

The energy exchange term in the gas-phase energy equation

$$S_h = \iiint f\left\{m_p\left[D_p(\boldsymbol{u}_p - \boldsymbol{u}_g)^2 - C_V\frac{dT_p}{dt}\right] - \frac{dm_p}{dt}\left[h_p + \frac{1}{2}(\boldsymbol{u}_p - \boldsymbol{u}_g)^2\right]\right\} dm_p d\boldsymbol{u}_p dT_p$$

Table 2
Particle-phase governing equations.

Transport equation of the particle distribution function *f*

$$\frac{\partial f}{\partial t} + \nabla_x\cdot(f\boldsymbol{u}_p) + \nabla_{\boldsymbol{u}_p}\cdot\left(f\frac{d\boldsymbol{u}_p}{dt}\right) = \frac{f_D - f}{\tau_D} + \frac{f_G - f}{\tau_G}$$

Particle acceleration equation

$$\frac{d\boldsymbol{u}_p}{dt} = D_p(\boldsymbol{u}_g - \boldsymbol{u}_p) - \frac{1}{\rho_p}\nabla p + \boldsymbol{g} - \frac{1}{\varepsilon_p \rho_p}\nabla\tau_p + \frac{\overline{\boldsymbol{u}_p} - \boldsymbol{u}_p}{\tau_D}$$

Particle phase volume fraction

$$\varepsilon_p = \iiint f \frac{m_p}{\rho_p} dm_p d\boldsymbol{u}_p dT_p$$

Particle motion equation

$$\frac{dx_p}{dt} = \boldsymbol{u}_p$$

Particle normal stress

$$\tau_p = \frac{P_s \varepsilon_p^{\beta}}{\max[\varepsilon_{cp} - \varepsilon_p, \delta(1-\varepsilon_p)]}$$

Particle phase energy equation

$$C_V\frac{dT_p}{dt} = \frac{1}{m_p}\frac{\lambda_g Nu}{d_p} A_p (T_g - T_p)$$

Gidaspow drag model

$$D_p = \begin{cases} D_1 & \varepsilon_p < 0.75\varepsilon_{cp} \\ (D_2 - D_1)\left(\dfrac{\varepsilon_p - 0.75\varepsilon_{cp}}{0.85\varepsilon_{cp} - 0.75\varepsilon_{cp}}\right) + D_1 & 0.75\varepsilon_{cp} \leq \varepsilon_p \leq 0.85\varepsilon_{cp} \\ D_2 & \varepsilon_p > 0.85\varepsilon_{cp} \end{cases}$$

$$D_1 = \frac{3}{8} C_d \frac{\rho_g}{\rho_p} \frac{|\boldsymbol{u}_g - \boldsymbol{u}_p|}{r_p}$$

$$D_2 = \left(\frac{C_1 \varepsilon_p}{\varepsilon_g Re} + C_2\right) \frac{\rho_g |\boldsymbol{u}_g - \boldsymbol{u}_p|}{\rho_p d_p}$$

$$C_d = \begin{cases} \dfrac{24}{Re}\varepsilon_g^{-2.65} & Re < 0.5 \\ \dfrac{24}{Re}(1 + 0.15Re^{0.687})\varepsilon_g^{-2.65} & 0.5 \leq Re \leq 1000 \\ 0.44\varepsilon_g^{-2.65} & Re > 1000 \end{cases}$$

compounds in the fuel may not decompose completely in the pyrolysis stage, and remain partially in the char. In this model, it is assumed that a portion of the nitrogen and sulfur remains in the char ($CN_{0.123}S_{0.012}(s)$), also leading to the production of SO_2 and NO, which is consistent with the actual situation. According to relevant research [18,19], the Boudouard reaction and water–gas reaction are primary as they have a substantial impact on the yield of the calorific gases CO and H_2. The oxy-fuel gasification of poultry manure involves a complex network of potentially hundreds of reactions. However, capturing every possible reaction in simulation of an industrial-scale gasification process is currently elusive. Our current model strategically includes 24 key reactions. The detailed chemical reactions and reaction rate equations are shown in Table 3.

2.2. Model validation

Our gasification physical model is based on the downdraft fixed-bed gasifier in Acropower Pte. Ltd.'s chicken manure gasification power plant in Singapore. The plant includes sub units such as chicken manure drying, pelletizing, gasification, cooling and purification, and power generation. The chicken manure undergoes a pretreatment process before being fed into the gasifier reactor, *i.e.*, it is dried in rotary drum dryers until it contains 10% moisture and then pelletized into manure pellets. The gasifier can process 750 kg of dry chicken manure per hour, and the generated syngas is cooled and purified before being sent to the internal combustion engine for combustion and power generation, and the produced biochar is discharged at regular intervals. Table 4 presents the ultimate and proximate analysis of dry chicken manure and biochar. Table 5 shows the specified inorganic species of dry chicken manure and biochar. In Tables 4 and 5, the analyses are for chicken manure that has been dried and pelletized prior to gasification.

It was found that the Ca content in chicken manure was high, which belongs to the alkaline earth metals and can have an impact on the emission of sulfur-containing pollutants [20]; therefore, we considered the self-desulfurization effect in the modeling process.

The photograph and physical model of the downdraft fixed-bed gasifier is shown in Fig. 1. The main body of the furnace is 3100 mm high and 2320 mm in diameter, and the char bed occupies about 75% of the height of the gasifier during steady operation. Both the feedstock and the gasifying agent are introduced from the top of the gasifier continuously. The feeding port is not sealed, which makes it easy to realize continuous charging, monitoring of the material layer, and operations such as stoking during runtime. The feeding rate of dry chicken manure is 750 $kg \cdot h^{-1}$. For plant operation, the gasifying agent used is air at room temperature and pressure, with a simulated density set at 1.164 $kg \cdot m^{-3}$. The gas supply fan is located at the rear of the gasifier, creating a slightly negative pressure inside the gasifier. Therefore, the gas flow rate is regulated by the pressure difference between the gasifier outlet and inlet, rather than by controlling the gas flow at the inlet. The flow rate of the cooled syngas is 800–850 $m^3 \cdot h^{-1}$ when the plant was in stable operation. The solid product, biochar, is discharged from the gasifier in batches. At regular intervals, biochar is transferred to a temporary storage tank *via* a discharge screw.

Under stable conditions, the composition of the syngas produced is 14.7% CO, 15.9% CO_2, 1.7% CH_4, 13.8% H_2, 0.9% O_2, and 50.9% N_2. As shown in the photograph, there are three temperature measurement points on the gasifier. During stable operation, from top to bottom, T_1 is 350 K, T_2 is 1034 K, and T_3 is 1079 K. T_1, T_2, and T_3 are located at heights of 370, 750, and 1120 mm from the top of the

Table 3
Chemical reaction rate expressions and kinetic parameters.

Chemical reactions	Reaction rate r and coefficient k
$CH_4 + 0.5O_2 \rightarrow CO + 2H_2$	$r = kC_{CH_4}^{0.5} C_{O_2}^{1.25}$ $k = 4.4 \times 10^{11}\exp(-1.26 \times 10^8/RT)$
$CH_4 + H_2O \rightarrow CO + 3H_2$	$r = kC_{CH_4} C_{H_2O}$ $k = 3.0 \times 10^8\exp(-1.26 \times 10^8/RT)$
$H_2 + 0.5O_2 \rightarrow H_2O$	$r = kC_{H_2} C_{O_2}^{0.5}$ $k = 5.69 \times 10^{11}\exp(-1.465 \times 10^8/RT)$
$CO + H_2O \rightarrow H_2 + CO_2$	$r = kC_{CO} C_{H_2O}$ $k = 2.75 \times 10^9\exp(-8.36 \times 10^7/RT)$
$CO + 0.5O_2 \rightarrow CO_2$	$r = kC_{CO} C_{O_2}^{0.5}$ $k = 5.62 \times 10^{12}\exp(-16000/T)$
$Tar + n_1O_2 \rightarrow n_2H_2O + n_3CO$	$r = kC_{Tar}^{0.5} C_{O_2}$ $k = 2.9 \times 10^5 T\exp(-9650/T)$
$Char + O_2 \rightarrow CO + SO_2 + NO$	$r = kC_{O_2}$ $k_9 = 2.30T\exp(-11100/T)$
$Char + O_2 \rightarrow CO_2 + SO_2 + NO$	$r = kC_{O_2}$ $k = 4.34 \times 10^7 \varepsilon_p T\exp(-1.13 \times 10^8/RT)$
$Char + CO_2 \rightarrow CO + SO_2 + NO$	$r = kC_{CO_2}$ $k = 589T\exp(-26800/T)$
$Char + H_2O \rightarrow H_2 + CO + SO_2 + NO$	$r = kC_{H_2O}$ $k = 5.714T\exp(-15600/T)$
$Char + 2H_2 \rightarrow CH_4$	$r = kC_{H_2}$ $k = 3.42 \times 10^{-3} T\exp(-15600/T)$
$HCN + 0.75O_2 \rightarrow CNO + 0.5H_2O$	$r = kC_{HCN} C_{O_2}$ $k = 2.14 \times 10^8\exp(-10000/T)$
$CNO + 0.5O_2 \rightarrow NO + CO$	$r = kC_{HCN} C_{O_2} \dfrac{k_a}{k_a + k_b C_{NO}}$ $k = 2.14 \times 10^8\exp(-10000/T)$ $k_b/k_a = 1.02 \times 10^{12}\exp(-25499/T)$
$CNO + NO \rightarrow N_2O + CO$	$r = kC_{HCN} C_{O_2} \dfrac{k_b}{k_a + k_b C_{NO}}$ $k = 2.14 \times 10^8\exp(-10000/T)$ $k_b/k_a = 1.02 \times 10^{12}\exp(-25499/T)$
$N_2O + CO \rightarrow N_2 + CO_2$	$r = kC_{N_2O} C_{CO}$ $k = 2.51 \times 10^{11}\exp(-23180/T)$
$N_2O \rightarrow N_2 + 0.5O_2$	$r = kC_{N_2O}$ $k = 1.75 \times 10^8\exp(-23180/T)$
$NH_3 + 0.75O_2 \rightarrow 0.5N_2 + 1.5H_2O$	$r = kC_{NH_3} C_{O_2}$ $k = 5.07 \times 10^{14}\exp(-35200/T)$
$NH_3 + 0.25O_2 + NO \rightarrow N_2 + 1.5H_2O$	$r = kC_{NH_3}^{0.5} C_{O_2}^{0.5} C_{NO}^{0.5}$ $k = 3.38 \times 10^{13}\exp(-29400/T)$
$NO + CO \rightarrow 0.5N_2 + CO_2$	$r = k\left[\dfrac{182.6C_{NO}(7.86C_{CO} + 0.002531)}{182.6C_{NO} + 7.86C_{CO} + 0.002531}\right]$ $k = 1.95 \times 10^{10}\exp(-19000/T)$
$NH_3 + 1.25O_2 \rightarrow NO + 1.5H_2O$	$r = kC_{NH_3} C_{O_2}$ $k = 3.1 \times 10^8\exp(-10000/T)$
$Char + NO \rightarrow N_2 + CO + SO_2$	$r = \dfrac{6\varepsilon_s \rho_s Y_c}{d_s \rho_c} kC_{NO}$ $k = 5.85 \times 10^7\exp(-12000/T)$
$Char + N_2O \rightarrow N_2 + CO + SO_2$	$r = \dfrac{6\varepsilon_s \rho_s Y_c}{d_s \rho_c} kC_{N_2O}$ $k = 1.74 \times 10^{10}\exp(-16983/T)$
$H_2S + 1.5O_2 \rightarrow H_2O + SO_2$	$r = kC_{H_2S} C_{O_2}$ $k = 5.2 \times 10^8\exp(-19300/RT)$
$CaO + SO_2 + 0.5O_2 \rightarrow CaSO_4$	$r = \dfrac{\varepsilon_s \rho_s Y_{CaO}}{\rho_{CaO}} \eta k C_{SO_2}$ $k = 1.1 \times 10^6\exp(-0.595 \times 10^8/RT)$ $\eta = \exp(-5.71X)$ $X = C_{CaSO_4}/(C_{CaO} + C_{CaSO_4})$

Table 4
Ultimate and proximate analysis of dry chicken manure (dry CM) and biochar.

	Proximate analysis/%				Ultimate analysis/%				
	M_{ad}	A_{ad}	V_{ad}	FC_{ad}	C_{ad}	H_{ad}	O_{ad}	N_{ad}	S_{ad}
Dry CM	9.02	25.86	45.24	19.88	30.90	4.54	24.95	3.63	1.10
Biochar	0	64.39	6.24	29.37	30.59	0.87	1.24	2.41	0.50

Table 5
Specified inorganic species analysis (% (mass)) of dry CM and biochar.

	Ca	Mg	K	Na	Zn	Mn	Fe	Cu	Si	Mo
Dry CM	7.42	0.81	2.38	0.24	0.03	0.03	0.44	<0.01	1.01	0.14
Biochar	20.51	1.41	4.12	0.42	0.05	0.05	0.83	<0.01	1.85	0.26

device, respectively. The model parameter settings in this work were based on the data during stable operation of the gasifier, as shown in Table 6. The Cartesian gridding method was used for gridding, and numerical simulations were conducted for 192774, 244032, 309672, 342792, and 390528 grid cell numbers to calibrate the grid sensitivity. As shown in Fig. 2, the simulated reactor pressure distribution results were similar when the number of grid cells was 342792, and 390528, whereas the calculation results using 192774, 244032, and 309672 grid cell numbers have significant differences. Therefore, considering the computational cost and simulation accuracy, the computational domain with a grid number of 342792 was selected. Whether the simulation has reached a quasi-steady state was determined by observing the changes in gasifier temperature and outlet syngas composition over time. Usually, the gasifier state has reached stability when the simulation time was 70 s. Therefore, the calculation time of each simulation case was set to 80 s, and the average value of 70 to 80 s was taken as the calculation result.

Table 6
Main operating and simulation parameters.

Initial gas in gasifier	100% N_2
Initial solid temperature/K	1023
Particle stacking volume fraction	0.58
Gasifying agent	Air and oxy-fuel atmosphere
CO_2 volume fraction in gasifying agent/%	21, 25, 30, 40, 50, 60
Syngas flow rate/$m^3 \cdot h^{-1}$	800–850
Inlet gasifying agent temperature/K	300
Gasifier pressure/MPa	0.1–0.5
Calculation time/s	80

In our series of work [13], the model has been successfully validated, and the accuracy of the model was confirmed by comparing the export syngas composition and gasifier temperature with operation data, including CO_2, CO, CH_4, N_2, H_2, T_1, T_2, T_3. Fig. 3 shows the comparison results between experimental data and simulation value. In order to display the errors of all parameters in Fig. 3, some data were scaled by multiplying by a factor. For example, the volume fraction of N_2 is approximately 50%, the $N_2 \times 0.1$ (%) represents the volume fraction value multiplied by 0.1. The results showed that the errors of the parameters were basically within 20%. This suggests that our model effectively captures the essential dynamics of the gasification process. Further, we extended the operating conditions to oxy-fuel gasification with CO_2

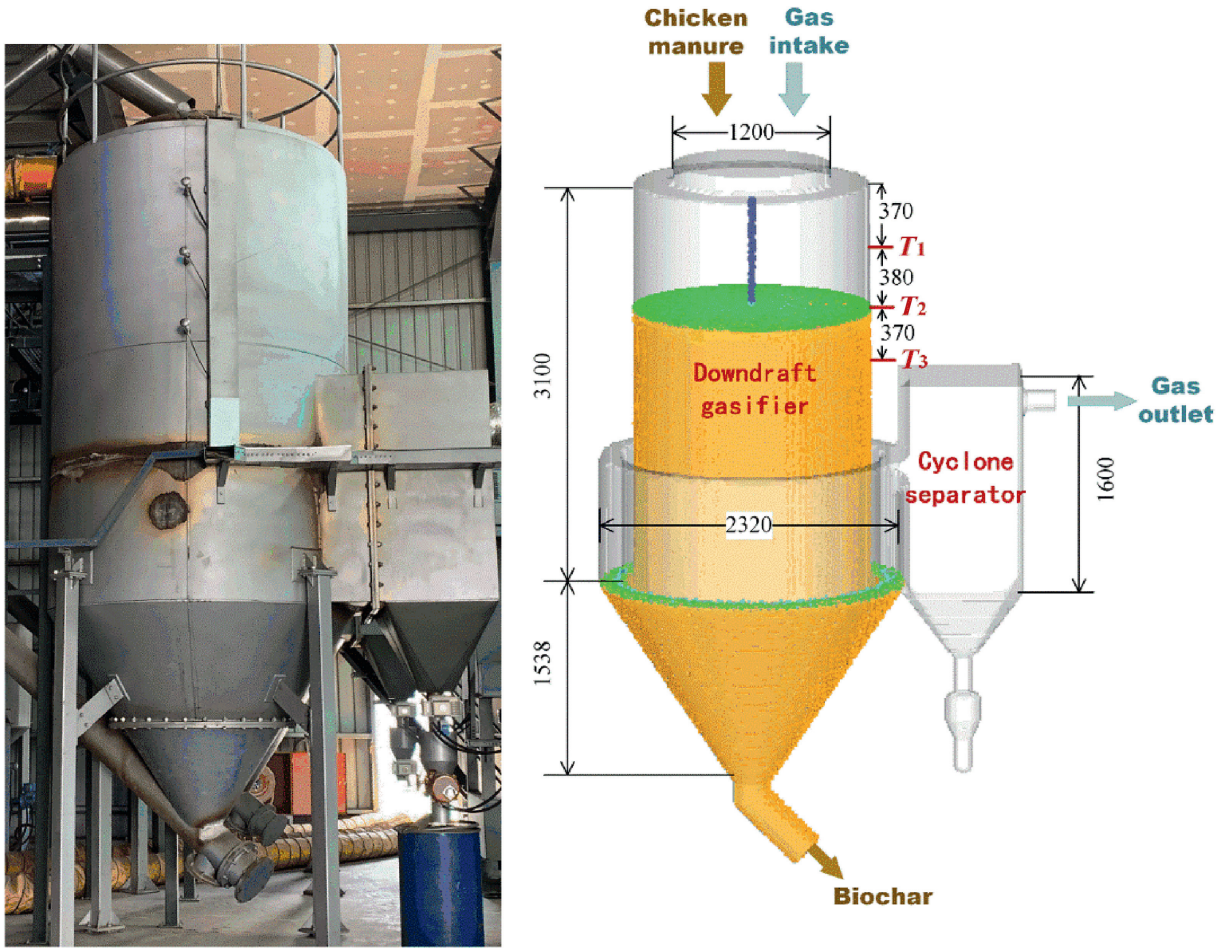


Fig. 1. Photograph and physical model of the downdraft fixed-bed gasifier.

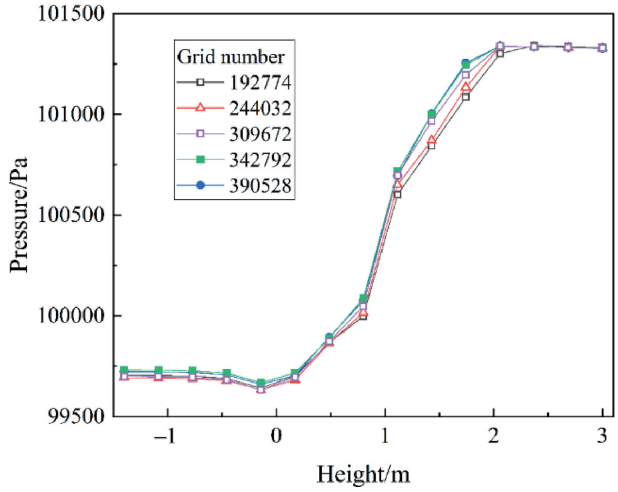


Fig. 2. Pressure distributions along the height in the gasifier reactor simulated with different number of grid cells.

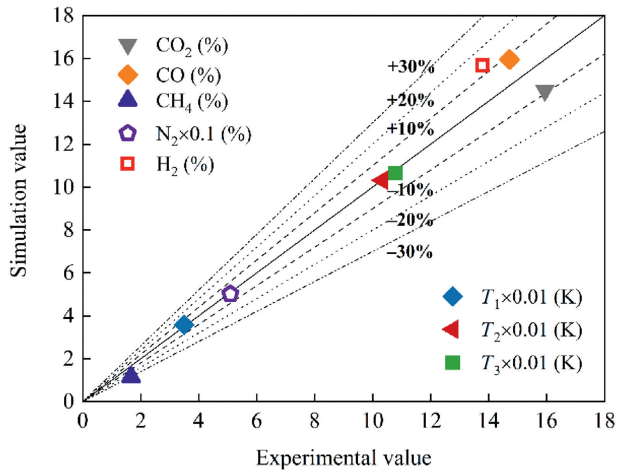


Fig. 3. Comparisons of experimental data and simulation value (including syngas composition and gasifier temperature).

percentages from 21% to 60% and gasification pressure from 0.1 to 0.5 MPa.

3. Results and Discussion

3.1. Effect of gasification pressure

At present, little is known about the pressurized gasification characteristics of biomass (poultry manure) in industrial-scale fixed-bed gasifiers, especially regarding the distribution of various parameter fields in gasifiers that are difficult to measure experimentally. Therefore, firstly, we discussed the changes of the calorific gas components CO, H_2, CH_4 and the most dominant component CO_2, including the composition of the outlet gas (dry flue gas) and the distribution of the concentration field in the gasifier (wet flue gas) when the gasification pressure (P) was increased from 0.1 to 0.5 MPa under the oxy-fuel condition (Oxy-30), as shown in Figs. 4 and 5, respectively. And the lower heating value (LHV) of syngas was calculated according to the following formula: $LHV_{gas} = LHV_{CO} \cdot c_{CO} + LHV_{H_2} \cdot c_{H_2} + LHV_{CH_4} \cdot c_{CH_4}$, where $LHV_{CO} = 12.64\ MJ \cdot m^{-3}$, $LHV_{H_2} = 10.79\ MJ \cdot m^{-3}$, $LHV_{CH_4} = 35.88\ MJ \cdot m^{-3}$. Regarding the reason for choosing Oxy-30

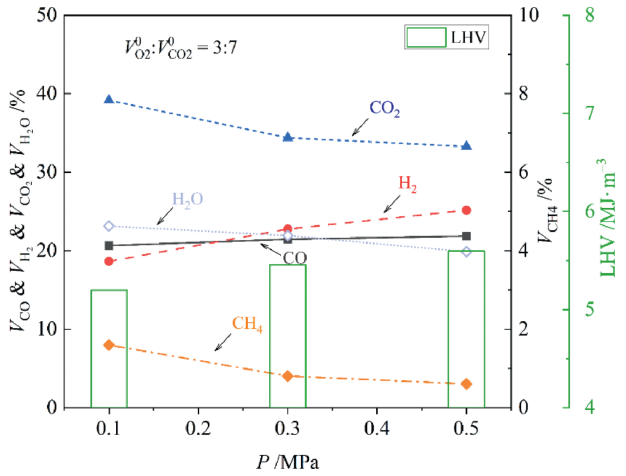


Fig. 4. The effects of gasification pressure (P) on the CO, H_2, CH_4, CO_2 concentrations and lower heating value of syngas.

as a typical oxy-fuel atmosphere in this work, our previous work has discussed the differences between atmospheric air gasification and oxy-fuel gasification, and found that the process efficiency of Oxy-21 gasification was slightly lower than that of air gasification, whereas the performance of Oxy-30 gasification was better. In addition, a number of studies on oxy-fuel combustion have concluded that the combustion performance under Oxy-30 conditions is comparable to, or even better than, that under air conditions. For example, Sher *et al.* [21] has pointed out that the oxygen volume concentration in the oxidant of O_2/CO_2 mixture had to be increased to 30% to keep a similar temperature profile to that achieved under the air combustion conditions.

As can be seen from Fig. 4, the concentration of the calorific gases CO and H_2 in the syngas increased with increasing pressure; while the concentration of the calorific gas CH_4 was approximately 1% and decreased with increasing pressure. CO_2 was both a gasifying agent and product, and it can account for up to 40% of the syngas under the Oxy-30 condition; the CO_2 concentration showed a decreasing tendency with increasing pressure. The H_2O concentration slightly decreased with increasing pressure, following the same trend as CO_2. This phenomenon is consistent with the results of some similar experimental studies. For example, Han *et al.* [4] investigated the effect of gasification pressure on H_2 production in a pressurized fluidized bed, using sawdust as feedstock and N_2 and steam as gasifying agents. Their data showed that increasing the reaction pressure favored higher H_2 fraction and yield and lower CO_2 fraction in the syngas. Xiao *et al.* [22] investigated pressurized air gasification and found that the concentrations of CO and H_2 increased with increasing pressure, while the concentrations of CH_4 and CO_2 remained almost unchanged. They attributed it to the enhanced gasification kinetics under elevated pressure and improved fluidization dynamics. In addition, our simulation data showed that when the pressure was increased from 0.1 to 0.3 MPa, the change in syngas composition was more significant, while the effect of pressurization was weaker when it was further increased to 0.5 MPa. For example, the CO concentrations at 0.3 and 0.5 MPa were almost the same.

Fig. 5(a)–(d) shows the comparison of 0.1 and 0.3 MPa at Oxy-30 under stable operation of the gasifier, including CO, H_2, CH_4, and CO_2, respectively. It can be seen that the CO concentration field exhibited an increase along the decrease in furnace height for both atmospheric and pressurized conditions, because the incomplete combustion and CO_2 reduction reactions in the oxidation and reduction section of the downdraft fixed bed led to the production

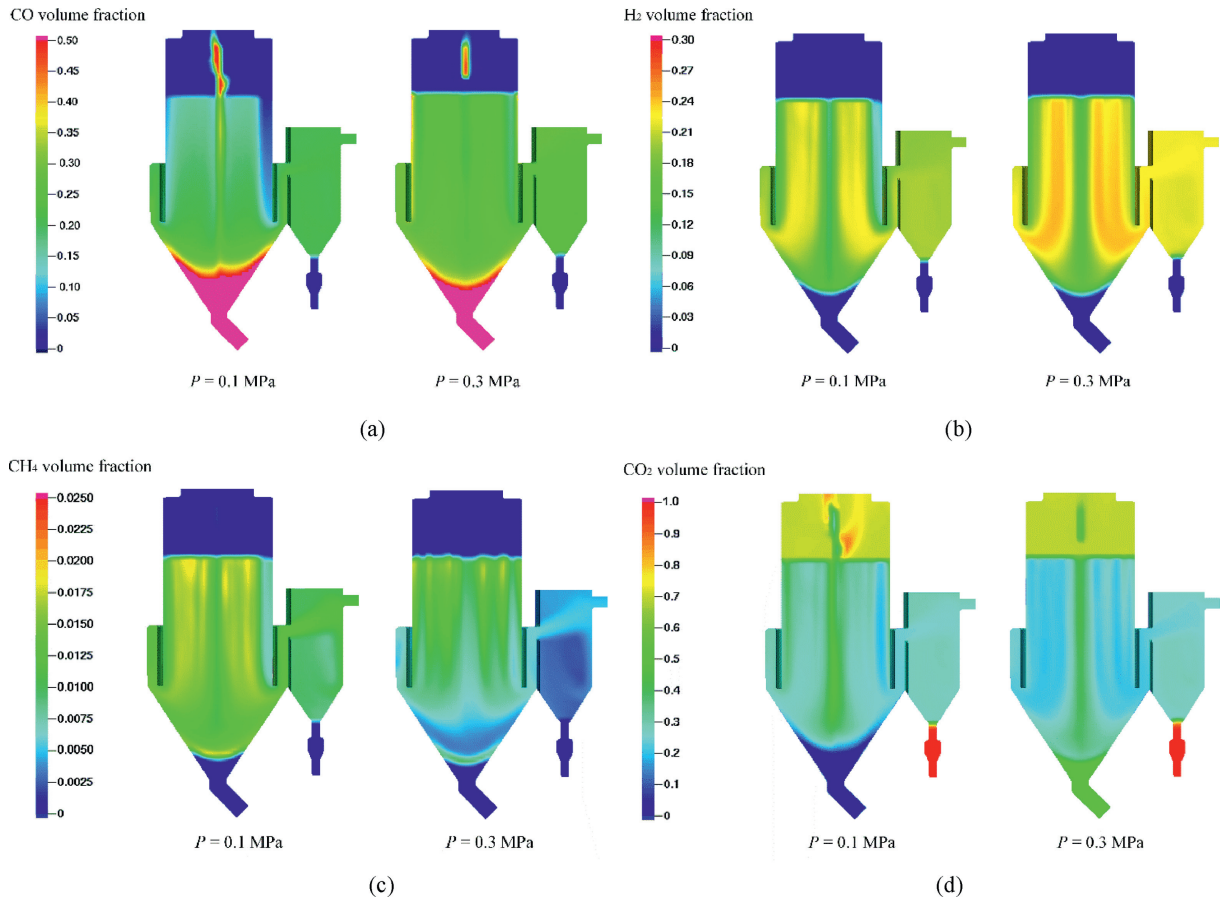


Fig. 5. Comparisons of 0.1 MPa and 0.3 MPa under Oxy-30 condition, including (a) CO, (b) H_2, (c) CH_4, and (d) CO_2.

of large amounts of CO. The relatively high concentration of CO near the top along the axis of the reactor was primarily due to chicken manure falling into the gasifier along this location. At this location, the chicken manure underwent rapid devolatilization to release CO. The phenomenon of a step transition of CO concentration from under 5% to around 20% near the top of the reactor was mainly influenced by the reactor temperature. Fig. 6 illustrates the variation of the average temperature in the radial direction along the axial direction. The temperature in the gas-phase zone was relatively low due to the influence of ambient air intake, and the CO in this zone mainly came from the devolatilization of chicken manure, which was relatively limited. In the solid-phase zone, the temperature of the char bed was generally around 1073 K, and the CO in this zone mainly came from the oxidation and reduction reactions of the feedstock, which generated a large amount of CO. Besides, the pressure condition seemed to have less effect on the CO concentration. Compared with the 0.1 MPa, the CO concentration in the gas-phase region was lower at 0.3 MPa, which was attributed to the suppression of the release of volatile substances by pressurization. The temperature profile showed that the temperature in the gas-phase region was also lower under pressurized condition, which may be due to the reduced release of combustible gases.

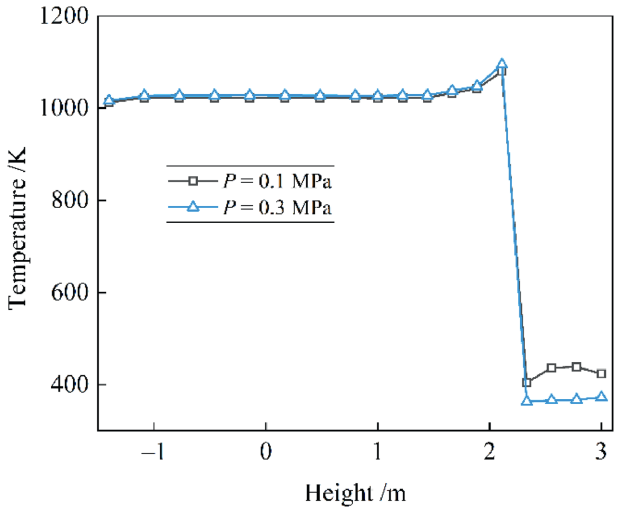


Fig. 6. Variations of the average temperature in the radial direction along the axial direction.

In contrast, as shown in Fig. 5(b) and (c), the H_2 concentration increased significantly under pressurized conditions. While the concentration of CH_4 decreased, which may be due to pressurization inhibiting the precipitation of volatile matter. Xiao *et al.* [22] pointed out that at conditions below 0.5 MPa, CH_4 mainly originated from volatile components rather than Char + $2H_2 \rightarrow CH_4$, so the promotion effect of pressurization on CH_4 generation was weak. Unlike conventional air gasification, the CO_2 concentration decreased along the furnace height during Oxy-30 gasification. This is because the CO_2 concentration at the inlet was as high as 70%, which was subsequently consumed in the Boudouard reaction. It can be seen that under pressurized conditions, the CO_2 concentration was lower both in the gas-phase section at the top of the furnace and in the bed layer filled with particles. This is because, on

the one hand, pressurization inhibits the release of volatiles in the pyrolysis stage, and on the other hand, it promotes the reaction between CO_2 and char and increases the gasification kinetics [23].

Overall, the pressurized condition increased the gasification kinetics, thus increasing the heating value of the syngas, as shown in Fig. 4. This may be because, on the one hand, the increase in operating pressure leads to a significant increase in the residence time of gas in the high-temperature reaction zone. Because according to the ideal gas law, an increase in gas pressure will result in an increase in gas density, which leads to a corresponding decrease in volumetric flow rate, *i.e.*, a decrease in the apparent gas velocity in the reactor. This promotes the gasification reaction, as shown in the following equation. If in order to maintain a consistent apparent gas velocity under increased pressure, it is necessary to increase the gas flow rate under pressurized conditions, which in turn will cause changes in the chemical stoichiometric ratio and thus affect the gasification process.

$$CN_{0.123}S_{0.012}(s) + O_2 \rightarrow CO + SO_2 + NO$$

$$CN_{0.123}S_{0.012}(s) + O_2 \rightarrow CO_2 + SO_2 + NO$$

$$CN_{0.123}S_{0.012}(s) + CO_2 \rightarrow CO + SO_2 + NO$$

$$CN_{0.123}S_{0.012}(s) + H_2O \rightarrow H_2 + CO + SO_2 + NO$$

Fig. 7 can demonstrate this flow phenomenon, showing the gas velocity vector (in the direction of the *Z*-axis direction, positive upward and negative downward) inside the downdraft fixed-bed gasifier. Fig. 7(a) is for the 0.1 MPa condition and Fig. 7(b) is for the 0.3 MPa condition. Firstly, it can be seen that the direction of gas flow in the main body of the furnace was generally from top to bottom and then upward through the annular channel into the cyclone separator. However, in the upper gas-phase area of the gasifier, there was an obvious phenomenon of gas flow back-mixing. It is noteworthy that the upward back-mixing was weakened under pressurized conditions compared to atmospheric pressure. In addition, in the solid-phase reaction zone, which was also the main reaction zone, the downward flow velocity of the gas flow decreased, thereby prolonging the contact time between the gas and particles.

On the other hand, pressurization is beneficial to gasification kinetics because pressurized conditions increase the concentration of reactants, thus increasing the reaction rate (according to the Arrhenius formula) and promoting the gasification reaction. Taking the reaction ($aA + bB \rightleftharpoons eE + fF$) as an example, the chemical reaction rate is calculated using $r = kC_A^m C_B^n$, and the reaction rate coefficient is calculated by $k = A \cdot \exp(-E/RT)$. The effect of pressure on the reaction rate is reflected by the change in reactant concentration. According to the gas state equation and Dalton's law of partial pressure, the chemical reaction rate equation is $r = kC_A^m C_B^n = k_G x_A^m x_B^n (p/RT)^{m+n}$. Where the reaction order ($m + n$) is greater than 1, so increasing the reaction pressure can accelerate the progress of the reaction.

Although only from the perspective of chemical reaction equilibrium, increasing the pressure is unfavorable to some gasification reactions. For example, when the pressure increases, the reaction $C + H_2O \rightarrow H_2 + CO$ moves in the direction of the reverse reaction, which is not conducive to the generation of CO. However, in a continuously fed gasifier, it is difficult for the reactions to reach equilibrium. The extension of residence time and the increase in reactant concentration brought about by pressurized conditions are beneficial for improving gasification kinetics and producing higher quality syngas. The effects of increased gasification pressure on syngas products are manifold. For example, an increase in pressure facilitates the methanation reaction $C + 2H_2 \rightarrow CH_4$ to produce CH_4, but at the same time pressurization inhibits the release of volatiles. At lower pressures, most of CH_4 in the syngas comes from volatiles. So it leads to a decrease in CH_4 concentration with increasing pressure. Therefore, from the perspective of the combined effect of chemical equilibrium and gasification reaction, the change in syngas is slowed down after the increase in pressure to a certain level.

3.2. Pollutant emissions

Due to the generally low temperature and limited oxygen provided during the gasification process, the syngas containing relatively low levels of nitrogen and sulfur pollutants can be produced, but the pollutants still cannot be eliminated. In particular, unlike

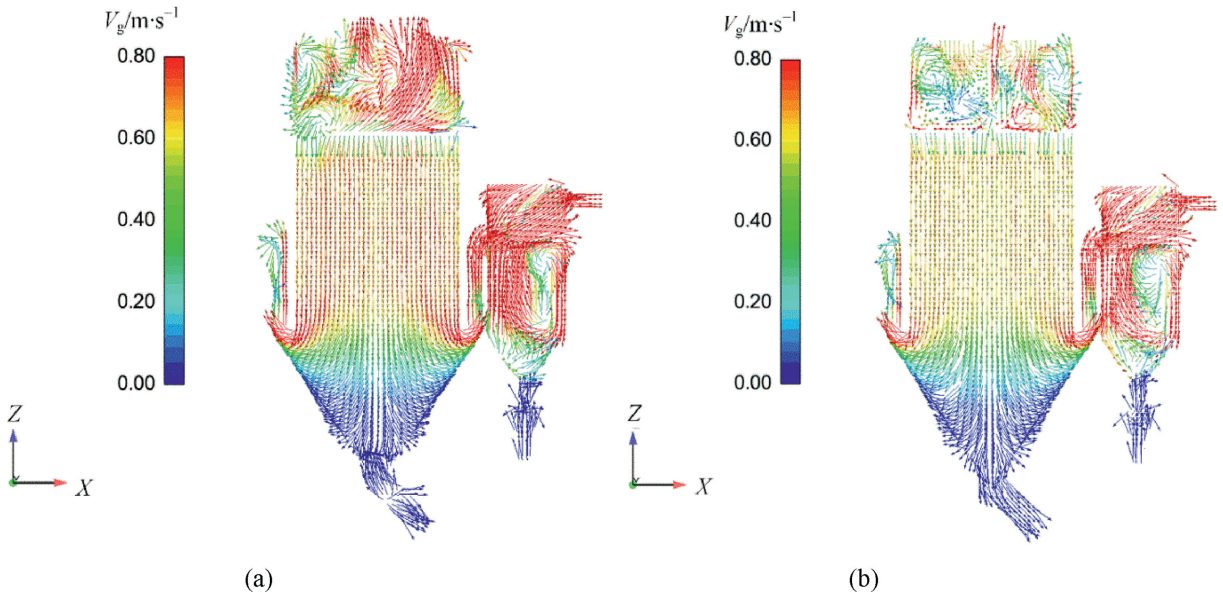


Fig. 7. Gas velocity vectors in the direction of the *Z*-axis direction inside the downdraft fixed-bed gasifier: (a) $P = 0.1$ MPa, (b) $P = 0.3$ MPa.

traditional agricultural and forestry biomass, livestock and poultry manure-type biomass itself has a higher nitrogen content due to the presence of proteins and amino acids. In this work, taking advantage of the numerical simulation method, the pressure effects targeting nitrogen and sulfur pollutants during oxy-fuel gasification were discussed, in order to provide a reference for the environmentally friendly utilization of livestock and poultry manure. This was rarely reported in the literature and few CFD numerical simulations of biomass gasification have considered the generation and transformation models for pollutants. However, due to computational power limitations, this model used global reaction kinetics to simulate the formation of N species, which may lead to relatively simple results. Because the global reaction kinetics model itself has the following limitations. The chemical reaction kinetics model is largely based on empirical formulas and experimental data. For complex non-linear reactions or atypical reactions, the model's predictive results may be inaccurate. Additionally, the parameters in the models usually need to be determined experimentally, which increases the difficulty of practical application of the models.

Fig. 8 shows the nitrogen-containing pollutants NH_3, HCN, and NO at pressures of 0.1 and 0.3 MPa during oxy-fuel gasification (Oxy-30). According to existing experimental research [24,25], it is known that the main gaseous nitrogen-containing products during biomass pyrolysis are HCN and NH_3, which are also the main precursors for NO generation. Depending on the availability of O_2, the generated NO is also reduced to N_2 homogeneously and heterogeneously. As can be seen from Fig. 8, the concentration of NO was very low compared to NH_3 and HCN in the gasification process of chicken manure. The concentrations of NH_3 and HCN were in the same order of magnitude, but HCN was slightly lower than NH_3. Because compared to coal, biomass tends to generate more NH_3 [26]. Surprisingly, as the pressure increased, the concentrations of both NH_3 and HCN increased, while the concentration of NO decreased. Similar phenomena have also been observed in some basic experiments on coal pyrolysis/combustion [27]. It was also found that pressurization can promote the release of fuel nitrogen in the pressurized oxy-fuel experiments with coal and biomass [20]. This suggests that pressurization promotes the conversion of fuel nitrogen and increases the yield of NO precursors (NH_3 and HCN). However, at the same time, the concentration of NO decreased with the increase of reaction pressure. This may be due to the fact that pressurization prolongs the syngas residence time and also promotes the reduction of NO by CO and char, as shown in the following equation, resulting in a decrease in NO concentration. As shown in Fig. 8(c), the NO concentration under pressurized conditions was lower in both the upper gas-phase space and the lower char bed region.

$$NO + CO \rightarrow 0.5N_2 + CO_2$$

$$CN_{0.123}S_{0.012}(s) + NO \rightarrow N_2 + CO + SO_2$$

Fig. 9 shows the distribution of SO_2 concentration under pressures of 0.1 and 0.3 MPa during oxy-fuel gasification (Oxy-30). It can be seen that the SO_2 concentration showed a decreasing trend with

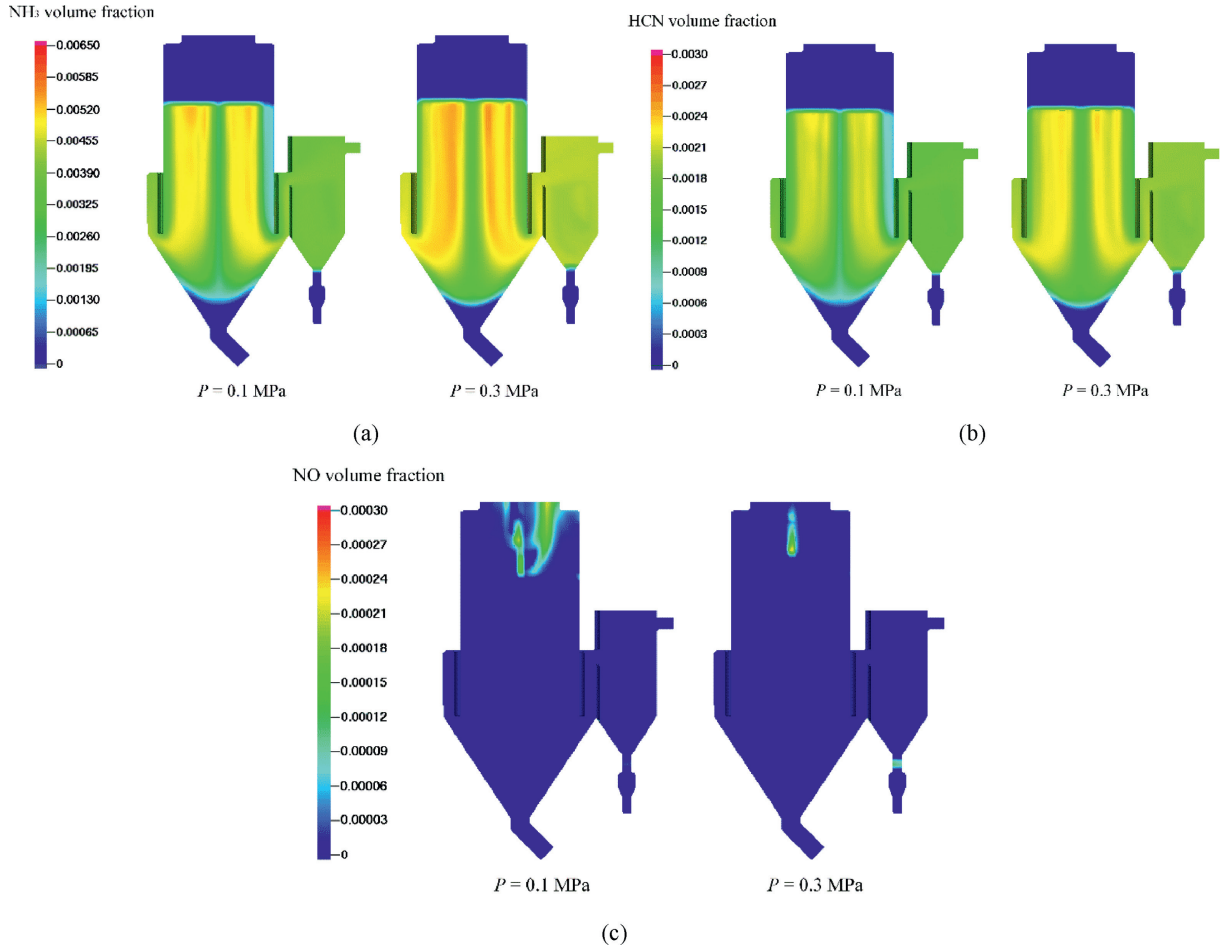


Fig. 8. (a) NH_3, (b) HCN, and (c) NO at pressures of 0.1 and 0.3 MPa during oxy-fuel gasification (Oxy-30).

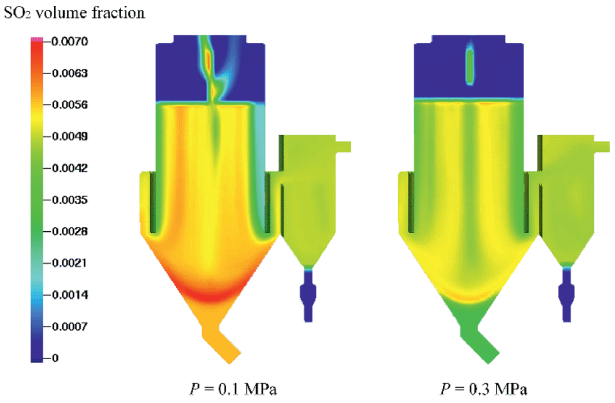


Fig. 9. SO_2 concentrations at pressures of 0.1 and 0.3 MPa during oxy-fuel gasification (Oxy-30).

the increase of gasification pressure, especially in the combustion and reduction section of the gasifier. Liang *et al.* [28] conducted pressurized oxy-fuel pyrolysis of pulverized coal in a laboratory-scale pressurized tubular furnace with an atmosphere of CO_2 with 99.99% purity, and the experimental data also showed that the main sulfur-containing pyrolysis gaseous products all decreased with increasing pyrolysis pressure. The possible reason for this phenomenon is that the increase in pressure decreases the apparent gas velocity, which prolongs the residence time of SO_2 in the flue gas on the surface of the char and ash particles, providing favorable conditions for self-desulfurization, and thus decreasing the SO_2 concentration. According to Grubor *et al.* [29], the self-desulfurization process is that the generated SO_2 may react with alkali metals and alkaline earth metals remaining in the ash to form sulfates, as shown in the following equation. And the self-desulfurization process mainly occurs during the combustion of char. Overall, the final concentration of sulfur-containing products is determined by

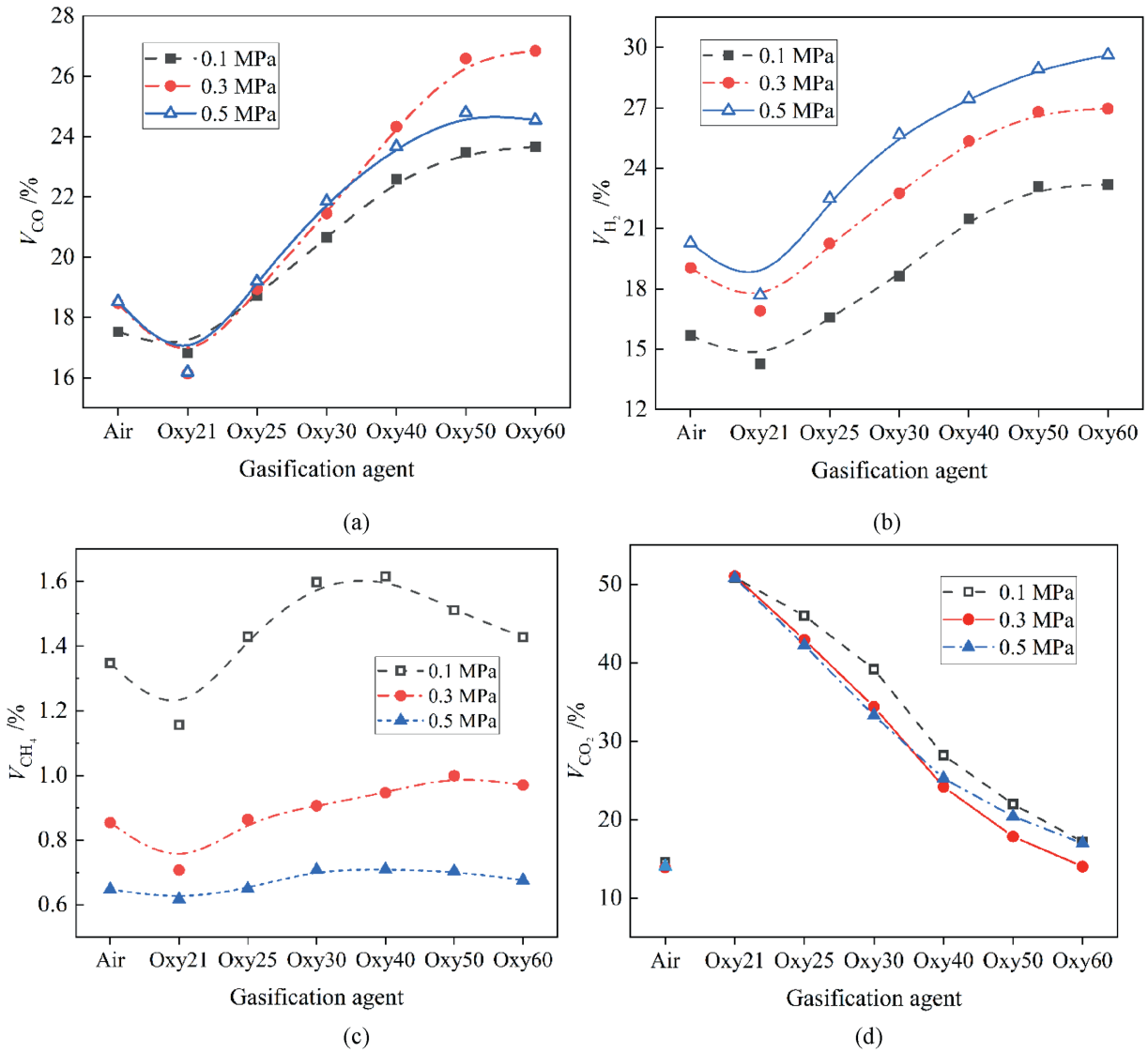


Fig. 10. (a) CO, (b) H_2, (c) CH_4, and (d) CO_2 concentrations with air and Oxy-21, Oxy-25, Oxy-30, Oxy-40, Oxy-50, and Oxy-60 as gasify agenting at operating pressures of 0.1–0.5 MPa.

complex interactions between various substances, and more mechanistic studies are needed to gain a deeper understanding.

$$CaO + SO_2 + 0.5O_2 \rightarrow CaSO_4$$

3.3. Effect of oxy-fuel atmosphere

Next, the effects of different oxy-fuel atmospheres (different O_2/CO_2 ratios) under different operating pressures on the gasification products and the coupling mechanism between them were further discussed. Fig. 10(a)–(d) shows CO, H_2, CH_4, and CO_2 concentrations with air and Oxy-21, Oxy-25, Oxy-30, Oxy-40, Oxy-50, and Oxy-60 as gasify agenting at operating pressures of 0.1–0.5 MPa, respectively. It can be found that for the products CO, H_2, and CH_4, the concentrations were higher under air gasification conditions than that of Oxy-21, even at different pressures. On one hand, this is because compared to N_2, CO_2 has a higher heat capacity. On the other hand, the activation of the Boudouard reaction along with other endothermic reactions is a key reason for the fact that the CO_2 reactions (reduction) is also triggered at prevailing temperatures compared to the N_2 reactions (which occur at much higher temperatures). These resulting in a slight decrease in reactor temperature, which in turn affects the conversion of feedstock.

For the product CO, as shown in Fig. 10(a), when the oxygen concentration did not exceed Oxy-30, the concentration of CO increased with the increase of pressure; but when the oxygen concentration exceeded Oxy-40, the concentration of CO decreased instead when the pressure was increased from 0.3 to 0.5 MPa. This may be due to the fact that the oxidation of CO is improved under the conditions of high oxygen and high pressure, where CO consumption dominates over CO generation. The higher oxygen concentrations are more favorable for $CO + 0.5O_2 \rightarrow CO_2$. In this case, further improving the pressure can significantly enhance this reaction to consume CO. The opposite effect of pressure on CO has also been observed in different existing research. For example, the experimental study by Han *et al.* [4] found that the CO concentration decreased with the increase of gasification pressure, while the experimental data of Xiao *et al.* [22] showed the opposite pattern. This also reflects that the mechanism by which pressure affects CO is complex.

In addition, under atmospheric pressure conditions, the CO concentration increased rapidly in the oxygen concentration interval from Oxy-30 to Oxy-40, and then the growth rate slowed down; whereas, under 0.3 MPa condition, the growth remained relatively rapid in the interval from Oxy-40 to Oxy-50. This may be because pressurization promotes the gasification reaction and the dominant gasification reactions that produce calorific gases H_2 and CO, such as Boudouard reaction and steam gasification reaction, are endothermic and energy-intensive. Higher oxygen concentration can provide more heat through the oxidation reaction to maintain a stable fixed-bed autothermal gasification. Therefore, compared with atmospheric pressure conditions, a relatively higher oxygen concentration is more favorable for autothermal gasification under pressurized conditions. Overall, the highest CO concentration was found around Oxy-50 for different pressure conditions. This is slightly higher than the expected range of oxygen concentration. This may be because for this commercial-scale fixed-bed gasifier, a large amount of feedstock was accumulated in the bed layer and the feed rate was fast, so more oxygen was required.

Compared to CO, the change trend of H_2 with oxygen concentration and pressure was clearer, as shown in Fig. 10(b). As the gasification pressure increased from 0.1 to 0.5 MPa, the concentration of H_2 increased continuously, and the increase was larger at lower pressures. Mühlen *et al.* [30] also pointed out that at relatively low pressures, the gasification reactivity increased linearly with increasing reaction pressure, however, at higher pressures, the effect of reaction pressure on gasification reactivity was no longer significant. As the gasification atmosphere was switched from air to Oxy-21 and then the oxygen concentration was gradually increased, the concentration of H_2 first decreased and then increased. Overall, the most significant improvement was observed within the range of Oxy-25 to Oxy-40.

Although the volume concentration of CH_4 was very low, it also showed a certain change rule with pressure and oxygen concentration, as shown in Fig. 10(c). First, the concentration of CH_4 decreased with the increase of pressure, and the pressure effect was obvious from 0.1 to 0.3 MPa. As the oxygen concentration increased from Oxy-21 to Oxy-60, the CH_4 concentration first increased and then decreased under 0.1 MPa, and reached its highest in the Oxy-30 and Oxy-40 interval. And under pressurized condition, the CH_4 concentration showed a similar change rule, but the highest concentration was between Oxy-40 and Oxy-50 interval, which has some similarity with the change rule of CO. This indicates that in order to maintain stable autothermal gasification and improve the gasification efficiency as much as possible, the oxygen-enriched concentration should be controlled in an appropriate range.

As shown in Fig. 10(d), air gasification produced approximately 15% CO_2, while oxy-fuel gasification produced a higher concentration of CO_2 in the syngas because CO_2 was used instead of N_2 in the gasification agent. But the concentration of CO_2 gradually decreased as the oxygen-enriched concentration increased. Overall, the CO_2 concentration under pressurized condition was lower than that at atmospheric pressure, but there may also be fluctuations. For example, when the oxygen concentration was lower than Oxy-30, it conformed to this change pattern. When the oxygen concentration reached Oxy-40, Oxy-50, and Oxy-60, the CO_2 concentration increased instead when the pressure was further increased from 0.3 to 0.5 MPa. This corresponds to the changes in CO mentioned earlier, which confirms that the oxidation of CO to produce CO_2 is promoted under the conditions of high oxygen and high pressure.

Finally, the lower heating value of syngas under different operating conditions is shown in Fig. 11. It is found that when the oxygen concentration exceeded Oxy-40, at this point, further pressure increase was no longer beneficial to the calorific value of

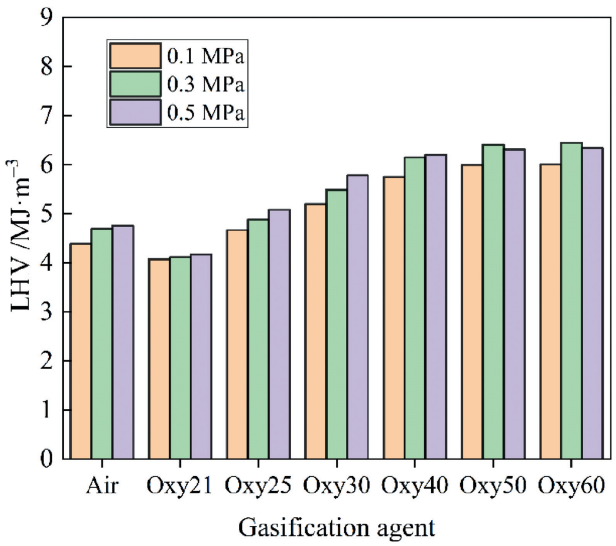


Fig. 11. Lower heating values of syngas under Oxy-21, Oxy-25, Oxy-30, Oxy-40, Oxy-50, and Oxy-60 at operating pressures of 0.1–0.5 MPa.

the syngas, and 0.3 MPa seemed to be a reasonable operating pressure. In addition, considering the cost of oxygen production, Oxy-40 was also a good choice, at which point the syngas calorific value was higher and already close to that of Oxy-50 and Oxy-60.

4. Conclusions

In this work, based on an industrial-scale chicken manure gasification power plant operating commercially in Singapore, an interesting first exploration for the coupled pressurization technology for the oxy-fuel gasification of livestock manure (chicken manure) was carried out through the construction of a 3D CFD numerical model under the MP-PIC framework. The operating pressure and oxygen-enriched concentration effects as well as the coupling mechanism between them in an industrial-scale downdraft fixed-bed gasifier were analyzed, and the conversion and emission of nitrogen- and sulfur-containing pollutants in the process were discussed, in order to provide a reference for the realization of a highly efficient and low-energy-consumption thermochemical treatment of livestock manure coupled with negative carbon emission technology. The main findings are as follows:

(1) Under oxy-fuel gasification condition (Oxy-30), as the operating pressure increases, the concentration of CO and H_2 in the syngas increases, while the CH_4 concentration decreases, resulting in an overall increase in the calorific value of syngas. CO_2 serves as both a gasifying agent and a product, and its concentration decreases with increasing pressure. The extended residence time and increased concentration of reactants brought about by the pressurized conditions are beneficial for improving gasification kinetics and producing higher quality syngas.
(2) With the increase of operating pressure, the concentrations of both NH_3 and HCN during the chicken manure gasification process increases, while the concentration of NO decreases. Pressurization promotes the fuel nitrogen conversion and increases NO precursors production, while also promoting homogeneous and heterogeneous reduction of NO. SO_2 concentration also decreases with increasing gasification pressure, probably because pressurization provides favorable conditions for self-desulfurization.
(3) Compared to atmospheric pressure conditions, a relatively higher oxygen-enriched concentration interval (Oxy-40 to Oxy-50) under pressurized conditions is advantageous for autothermal gasification. However, when the oxygen concentration exceeds Oxy-40, further increasing the pressure from 0.3 to 0.5 MPa may lead to a decrease in the calorific value of syngas. Compared to CO and CH_4, the tendency of H_2 to increase with increasing oxygen concentration and pressure is more stable.

CRediT Authorship Contribution Statement

Qinwen Liu: Writing – original draft. Guoqing Lian: Supervision. Wenli Dong: Supervision. Yu Su: Supervision. Wei Quan Leong: Supervision. Chi-Hwa Wang: Supervision. Wenqi Zhong: Supervision.

Declaration of Competing Interest

The authors declare that they have no known competing financial interests or personal relationships that could have appeared to influence the work reported in this paper.

Acknowledgements

This research is supported by the National Natural Science Foundation of China (52306131), the Natural Science Foundation of Jiangsu Province (BK20230847), the Key Project of the National Natural Science Foundation of China (52336005), and the Fundamental Research Funds for the Central Universities (2242024RCB0036), and the Open Project Program of State Key Laboratory of Low-carbon Smart Coal-fired Power Generation and Ultra-clean Emission (D2024FK156).

Nomenclature

C_V	specific heat of the particle material
D	turbulent mass diffusivity
D_p	drag function
$\boldsymbol{F}$	inter-phase momentum transfer rate per unit volume
$\boldsymbol{g}$	gravity
h_g	fluid enthalpy
p	fluid pressure
Q	energy source per volume
$\boldsymbol{q}$	fluid heat flux
q_D	enthalpy diffusion term
R	universal gas constant
S_h	conservative energy exchange from the particle phase to the fluid phase
T_p	particle temperature
$\boldsymbol{u}_g$	fluid velocity vector
δ	a small number on the order of 10^{-7}
ε_g	fluid volume fraction
ε_p	solid volume fraction
λ_g	fluid thermal conductivity
τ_D	particle collision damping time
τ_g	fluid stress tensor
τ_p	solids contact stress
Φ	viscous dissipation

References

[1] A. Tawfik, M. Eraky, A.I. Osman, P. Ai, Z.B. Zhou, F.G. Meng, D.W. Rooney, Bioenergy production from chicken manure: a review, *Environ. Chem. Lett.* 21 (5) (2023) 2707–2727.
[2] X. He, Q. Hu, J.L. Chen, W.Q. Leong, Y.J. Dai, C.H. Wang, Energy and environmental risk assessments of poultry manure sustainable solution: an industrial case study in Singapore, *J. Clean. Prod.* 339 (2022) 130787.
[3] W.C. Ng, S.M. You, R. Ling, K.Y. Gin, Y.J. Dai, C.H. Wang, Co-gasification of woody biomass and chicken manure: syngas production, biochar reutilization, and cost-benefit analysis, *Energy* 139 (2017) 732–742.
[4] L. Han, Q.H. Wang, Z.Y. Luo, N. Rong, G.Y. Deng, H_2 rich gas production *via* pressurized fluidized bed gasification of sawdust with *in situ* CO_2 capture, *Appl. Energy* 109 (2013) 36–43.
[5] N. Spiegl, X.Y. Long, C. Berrueco, N. Paterson, M. Millan, Oxy-fuel co-gasification of coal and biomass for negative CO_2 emissions, *Fuel* 306 (2021) 121671.
[6] Y. Shi, W.Q. Zhong, Y.J. Shao, X.J. Liu, Energy efficiency analysis of pressurized oxy-coal combustion system utilizing circulating fluidized bed, *Appl. Therm. Eng.* 150 (2019) 1104–1115.
[7] L.P. Tan, L. Cai, Y.L. Xiang, Y.W. Guan, W.B. Liu, Investigation on oxy-fuel biomass integrated gasification combined cycle system with flue gas as gasifying agent, *Biomass Bioenergy* 166 (2022) 106621.
[8] G.Y. Zang, J.X. Jia, S. Tejasvi, A. Ratner, E. Silva Lora, Techno-economic comparative analysis of biomass integrated gasification combined cycles with and without CO_2 capture, *Int. J. Greenh. Gas Control* 78 (2018) 73–84.
[9] X.L. Zhu, Z.B. Wang, R. Ocone, H.G. Wang, MP-PIC simulation on CO_2 gasification of biomass in a pilot plant circulating fluidized bed gasifier, *Fuel* 332 (2023) 125992.
[10] M. Lei, Y.T. Zeng, D.K. Hong, Y.J. Hu, W. Liu, Q. Zhang, L. Zhang, Investigation on the emission characteristics of gaseous sulfur during pressurized coal gasification by experiment and ReaxFF MD stimulation, *J. Energy Inst.* 119 (2025) 101986.
[11] N. Samani, R. Khalil, M. Seljeskog, J. Bakken, R.K. Thapa, M.S. Eikeland, Experimental and simulation studies of oxygen-blown, steam-injected, entrained flow gasification of lignin, *Fuel* 362 (2024) 130713.

[12] Z.P. Yao, X.D. Song, S. Yan, Z.H. Xia, C.X. Chen, X. Qu, J.C. Bi, Numerical study in the pressure effects on coal catalytic hydrogasification in the bubbling fluidized bed, *Fuel* 346 (2023) 128383.
[13] Q.W. Liu, Y.Y. Wang, W.Q. Leong, Y.H. Gu, A. Lin, Y.C. Wang, A.B. Yu, W.Q. Zhong, C.H. Wang, Study of a commercial-scale poultry manure oxy-fuel gasification plant *via* CFD modeling and safety assessment, *Biomass Bioenergy* 185 (2024) 107248.
[14] A. Amani, F. Akhlaghian, Hydrogen production from co-gasification of Çan lignite and sorghum biomass in a fixed-bed gasifier: CFD modeling, *Int. J. Energy Environ. Eng.* 13 (1) (2022) 295–304.
[15] A. Klimanek, J. Bigda, CFD modelling of CO_2 enhanced gasification of coal in a pressurized circulating fluidized bed reactor, *Energy* 160 (2018) 710–719.
[16] D.M. Snider, S.M. Clark, P.J. O'Rourke, Eulerian–Lagrangian method for three-dimensional thermal reacting flow with application to coal gasifiers, *Chem. Eng. Sci.* 66 (6) (2011) 1285–1295.
[17] D.M. Snider, Three fundamental granular flow experiments and CPFD predictions, *Powder Technol.* 176 (1) (2007) 36–46.
[18] Y.P. Cheng, Z. Thow, C.H. Wang, Biomass gasification with CO_2 in a fluidized bed, *Powder Technol.* 296 (2016) 87–101.
[19] Y. Shen, X. Li, Z.Y. Yao, X.Q. Cui, C.H. Wang, CO_2 gasification of woody biomass: experimental study from a lab-scale reactor to a small-scale autothermal gasifier, *Energy* 170 (2019) 497–506.
[20] Q.W. Liu, W.Q. Zhong, A.B. Yu, C.H. Wang, Co-firing of coal and biomass under pressurized oxy-fuel combustion mode in a 10 kW_{th} fluidized bed: nitrogen and sulfur pollutants, *Chem. Eng. J.* 450 (2022) 138401.
[21] F. Sher, M.A. Pans, C.G. Sun, C. Snape, H. Liu, Oxy-fuel combustion study of biomass fuels in a 20 kW_{th} fluidized bed combustor, *Fuel* 215 (2018) 778–786.
[22] R. Xiao, M.Y. Zhang, B.S. Jin, Y.J. Huang, H.C. Zhou, High-temperature air/steam-blown gasification of coal in a pressurized spout-fluid bed, *Energy Fuels* 20 (2) (2006) 715–720.
[23] Q.W. Liu, W.Q. Zhong, A.B. Yu, C.H. Wang, Co-firing of coal and biomass under pressurized oxy-fuel combustion mode: experimental test in a 10 kW_{th} fluidized bed, *Chem. Eng. J.* 431 (2022) 133457.
[24] S. Liu, W. Cao, Y. Wang, W.W. Wei, L.H. Li, H. Jin, L.J. Guo, Characteristics and mechanisms of nitrogen transformation during chicken manure gasification in supercritical water, *Waste Manag.* 153 (2022) 240–248.
[25] C.Z. Li, L.L. Tan, Formation of NO_x and SO_x precursors during the pyrolysis of coal and biomass. Part III. Further discussion on the formation of HCN and NH_3 during pyrolysis, *Fuel* 79 (15) (2000) 1899–1906.
[26] M.J. Aho, J.P. Hämäläinen, J.L. Tummavuori, Importance of solid fuel properties to nitrogen oxide formation through HCN and NH_3 in small particle combustion, *Combust. Flame* 95 (1–2) (1993) 22–30.
[27] X.R. Liang, Q.H. Wang, Z.Y. Luo, E. Eddings, T. Ring, S.M. Li, P. Yu, J.Q. Yan, X.D. Yang, X. Jia, Experimental and numerical investigation on nitrogen transformation in pressurized oxy-fuel combustion of pulverized coal, *J. Clean. Prod.* 278 (2021) 123240.
[28] X.R. Liang, Q.H. Wang, Z.Y. Luo, E. Eddings, T. Ring, S.M. Li, L. Han, J.J. Lin, G.L. Xie, Experimental study on sulfur-containing products in pressurised oxy-fuel pyrolysis of pulverised coal, *J. Clean. Prod.* 279 (2021) 123818.
[29] B. Grubor, V. Manovic, S. Oka, An experimental and modeling study of the contribution of coal ash to SO_2 capture in fluidized bed combustion, *Chem. Eng. J.* 96 (1–3) (2003) 157–169.
[30] H.J. Mühlen, K.H. van Heek, H. Jüntgen, Influence of pretreatment temperature and pressure on the char reactivity during hydrogasification, *Fuel* 65 (4) (1986) 591–593.